Initial stages of AZ91 Mg alloy micro-arc anodizing: Growth mechanisms and effect on the corrosion resistance

Delphine Veys-Renaux, Emmanuel Rocca, J. Martin, Gérard Henrion

Initial stages of AZ91 Mg alloy micro-arc anodizing: growth mechanisms and effect on the corrosion resistance

Delphine VEYS-RENAUX*, Emmanuel ROCCA, Julien MARTIN, Gérard HENRION.

Institut Jean Lamour-UMR CNRS 7198, Université de Lorraine, BP 70239, Vandoeuvre-lès-Nancy, 54506, France.

**corresponding author:*

e-mail: delphine.veys-renaux@univ-lorraine.fr

phone: +33 3 83 68 46 30

fax : +33 3 83 68 46 11

Abstract:

In the framework of the new ecological regulations, micro-arc oxidation (MAO) appears as an alternative to usual processes in the field of corrosion protection of Mg alloys. In this work, the initial stages of anodic layer growth in KOH-based electrolytes are studied up to and beyond the initiation of the micro-arc regime.

The properties of the first anodized film preceding the occurrence of the dielectric breakdown (corresponding to the start of the micro-arc regime) are mainly determined by the incorporation of additives (fluorides or silicates) in the film, as shown by in situ electrochemical measurements. Scanning electron microscopy (SEM), X-Ray photoelectron spectroscopy (XPS) and micro-Raman spectroscopy reveal both the change of morphology and chemical state of silicate and fluoride in the anodized layer before and after the micro-arc regime. In terms of electrochemical behaviour, investigated by stationary methods and electrochemical impedance spectroscopy (EIS) in reference corrosive water, the anodic film grown in the silicate medium provides the best corrosion resistance thanks to a thick layer containing Mg_2SiO_4, whose degradation products seal the porosities of the coating.

Keywords: micro-arc anodizing**,** anodic film, EIS, corrosion

1. Introduction

In the framework of the reduction of energy consumption, magnesium alloys are more and more used in the aircraft industry. However the problem remains the high sensitivity of magnesium and its alloys to corrosion, especially pitting corrosion [1], so that surface treatments must be applied, generally by electrochemical conversion processes, leading to more protective coatings than chemical conversion processes as phosphatation [2-3] or chromatation [4]. In order to replace commercially developed anodizing processes such as HAE and DOW17 [5], micro-arc oxidation (MAO) appears as an interesting alternative since it consists of a single-step process that avoids the use of heavy metals as chromium or manganese. In this anodizing process, the application of high voltages in an alkaline electrolyte allows to exceed the dielectric breakdown voltage of the oxide [6], leading to the initiation of a sparking regime due to the formation of local dielectric discharges. Thanks to the high temperature reached within the plasma during this sparking phenomenon, the resulting anodic coatings are dry ceramic layers, exhibiting interesting tribological and anti-corrosion properties. These properties depend on all parameters of the anodizing process, namely the electrical parameters [7-10] and the composition of the electrolyte [10-15]. KOH-silicates or KOH-KF based solutions are generally used as electrolytic baths. Recent studies have shown that the electrochemical behavior and the corrosion resistance of the treated Mg alloys are very likely linked to the properties of a first insulating layer, formed before the dielectric breakdown by conventional anodizing [16, 17].

The purpose of this work is to precisely describe and understand of the initial stages of anodizing before and just after the dielectric breakdown in KOH-concentrated electrolyte containing or not fluorides and silicates. The anodizing process was monitored by in-situ electrochemical impedance measurements during a high voltage scans. The consequences of the local electric discharges on the growth and chemical transformation of the anodized layer were instigated by scanning electron microscopy (FEG-SEM), X-Ray photoelectron spectroscopy (XPS) and micro-Raman spectroscopy. The electrochemical behavior of the

layer before and after the initiation of the micro-arc regime was analyzed by stationary techniques and electrochemical impedance spectroscopy in corrosion condition.

2. Experimental

The growth of anodized coatings on AZ91 plates (circular mirror-like polished samples, area 3 cm^2) was performed by applying potentiodynamic scans from 0 to 75 V, with a scan rate of 100 mV s^{-1}, in KOH(3 mol L^{-1})-based electrolytic bathes. A three-electrode cell, connected to a Modulab HV100 potentiostat, was used with the studied sample as a working electrode, a saturated calomel electrode as a reference electrode and a platinum grid (area 5 cm^2) as a counter electrode. The effect of addition of fluorides (KF 0.5 mol L^{-1}) or silicates (Na_2SiO_3 0.5 mol L^{-1}) to the reference bath was investigated. The evolution of the electrochemical interface during polarization was in-situ characterized by continuous single-frequency impedance measurements (for f=5000 Hz). As described in a previous work [17], the results were interpreted in terms of film capacitance C and charge transfer resistance R, forming a loop in series with the electrolyte resistance.

Surface and electrochemical characterizations were then realized on samples anodized until 40 V and for samples anodized up to 75 V.

Morphology and thickness of the coatings were investigated by scanning electron microscopy (SEM) observations (HITACHI FEG-4800) of surface and cross-sections (with a metallographic preparation realized by an ionic cross-section polisher Jeol 09010). The coatings were characterized by X-ray photoelectron spectroscopy (XPS) with a Kratos AXIS Ultra DLD spectrometer after argon ion sputtering. The spectra were recorded by using a monochromatized Al-K_α X-ray radiation (1486.6 eV), with 20 eV pass-energy in the hemispherical analyser and a take-off angle of 90°. For internal calibration, C1s peak (285.0 eV) was used. Data analysis was carried out using CASA XPS software package. Integrated

Shirley backgrounds were employed [18] and the peaks were fitted using a 30% mix of Gaussian and Lorentzian line shapes.

The chemical analysis of the surface was completed by Raman spectroscopy measurements performed on the top-surface of each processed sample. Raman spectra were recorded in backscattered geometry using a micro-Raman spectrometer (LabRam Infinity®) developed by Horiba Jobin Yvon. Both the incident and the scattered lights were collected through an Olympus confocal microscope equipped with a 50x objective lens. Raman excitation was provided by an argon laser operating at 514 nm with a power of about 1.1 mW. Rayleigh scattered light is eliminated through a holographic notch. Before being detected by a Peltier cooled 2D-CCD detector, Raman scattered light was focused onto a 600 g/mm diffraction grating resulting in a spectral resolution of 1 cm^{-1}. All spectra were recorded in the range 40 to 1800 cm^{-1} and calibrated using the 520.5 cm^{-1} line of a silicon wafer. A micro-computer linked to the CCD allows recording spectra through Labspec® acquisition software (Horiba Jobin Yvon).

Electrochemical characterizations of the anodized samples were carried out with the three-electrode cell previously used for the anodizing process, but this time connected to a Gamry instruments Framework (600 Potentiostat / Frequency Response Analyser) in a reference corrosive solution (D 1384-87 ASTM standard water [19]: Na_2SO_4, 148 mg/l; $NaHCO_3$, 138 mg/l; NaCl, 165 mg/l (pH=8.3)), noted "ASTM water", whose composition simulates corrosion under atmospheric conditions [10, 16]. The following experimental sequence was used:

a) Measurement of the open-circuit potential (E_{corr}) during 22 h in ASTM corrosive water,
b) Every 2h during this duration, measurement of the electrochemical impedance spectra from 300 kHz to 5 mHz with a 20 mV amplitude. Impedance data were analysed with the ZSimpWin3.22 software, using a nonlinear least squares fitting routine [20].

c) Measurement of the anodic and cathodic polarization curves independently after 22h immersion in ASTM water with a scan rate of 1 mV s^{-1}.

3. Results

3.1. Anodizing process

The in-situ electrochemical characterization of the anodizing process at high voltages, presented in Fig. 1 and 2, reveals that the growth of the oxidized layer consists of two steps, separated by the initiation of electric discharges corresponding to the beginning of the so-called micro-arc regime (between 47 V and 62 V, depending on the electrolyte composition). Before this dielectric breakdown, a conventional anodizing mechanism results in the growth of a first insulating layer. By assuming that the C capacitance calculated from single frequency measurements (Fig. 2a) can be assigned to the dielectric properties of the oxidized layer ($C = \varepsilon\varepsilon_0/d$ with d the thickness of the anodic film) [17], the growth of the anodic film would be quasi-linear with the applied voltage. Whatever the electrolyte content, this conventional anodizing regime ends for a same value of capacitance (about 1.7 10^{-7} F cm^{-2}), which would correspond to a thickness of about 50 nm by assuming a substrate uniformly covered by MgO ($\varepsilon_0 = 10$). The addition of fluorides (0.5 mol L^{-1}) or silicates (0.5 mol L^{-1}) in the KOH electrolyte (3 mol L^{-1}) seems to slightly influence the growth rate of the anodic film but not the growth mechanism. However, the resistance R of the electrochemical interface during the conventional anodizing process (Fig.2b), which can be assigned to the charge transfer resistance [17], is modified by the additives in the electrolyte. Whereas this resistance remains constant in the KOH electrolyte (consistently with the linear increase of current density in Fig.1), the blocking properties of the anodic films grown in the fluoride-containing and silicate-containing electrolytes are improved (more in the case of fluorides addition) as revealed by the increase in R value and the low value of the current density measured during the process.

As soon as the discharges phenomenon has been initiated, the anodizing mechanism changes from an electrochemical point of view. According to the increasing values of 1/C and R with the voltage (hard to acquire and very noisy in these sparking conditions), the coatings keep on growing in presence of additives in the electrolyte, faster than under classical anodizing conditions. On the other hand, the growth would be stopped in pure KOH or counterbalanced by a high dissolution rate.

3.2. Surface analysis

In order to get a better understanding of the two growth mechanisms during the anodizing process and especially of the role of the additives during the classical anodizing regime and the micro-arc regime, surface characterizations were performed on samples anodized up to 40 V and up to 75 V.

3.1.1 Morphology and thickness of the coatings

As shown on an example in Fig. 3a, the thickness of the coating is about 200 nm for all samples anodized up to 40V. These measured thicknesses are higher than the thicknesses evaluated by the capacitance values calculated from the impedance measurements (about 40 nm with ε_0 = 10). This difference can be explained first by the assumption of a pure capacitance in the equivalent circuit used to fit the impedance results [21] and secondly by the effect of the morphology of the anodic films, influencing both ε_0 and the surface S. Actually, the oxide layers formed until 40 V are porous and made of tangled nano-plates as revealed by the high magnification pictures (Fig. 3b, 3c and 3d). The structure of the coatings grown in fluoride-containing or silicate-containing electrolytes is finer than in pure KOH, which could induce a better surface coverage and explain the higher charge transfer resistance measured during the anodizing process (Fig. 2b).

The effect of fluoride or silicate addition in KOH electrolyte is more important on the layer anodized up to 75 V. Indeed, in pure KOH electrolyte, the layer thickness increases only twofold between 40 V and 75 V, which is consistent with a linear growth between 40 V and

60 V followed by a stopping of the growth process from the dielectric breakdown (as indicated by the constant values of resistance and capacitance of the layer measured from 60 V in Figure 2).

On the contrary, in presence of fluoride or silicate additives, the thickness of the coatings increases respectively ten to hundred times between 40 V and 75 V. The resulting anodic film can be described as a stacking of (Fig. 4):

- a thin layer directly in contact with the substrate,
- an intermediate layer containing small porosities; some of them being closed, probably because of the oxygen bubbles formation by water oxidation at high voltages,
- and a top layer in which macro-cracks and big holes correspond to the discharges channels opened towards the electrolyte.

It is worth noting that at 75 V, the layer formed in KOH/Na_2SiO_3 electrolyte (about 20 µm) is much thicker that the one formed in KOH/KF electrolyte (about 2 µm). In fact, this observation can be explained by an intrinsic effect of the silicate additive compared to the fluoride one, but also by the difference of micro-arc regime duration. Indeed, the dielectric breakdown in silicates medium appears at lower voltage (around 47 V) than with fluorides (around 62 V). Consequently, the samples were exposed to the discharges regime during 5 min. in silicate-containing electrolyte and 2 min during the same voltage ramp of the anodizing process.

Moreover, the thicker layer is much rougher, and much larger channels appear on the surface corresponding to more energetic discharges, as previously reported by other studies [22].

3.1.2 Chemical characterization of the coatings

Samples anodized up to 40 V and 75 V were also compared in terms of chemical composition by XPS (Fig. 5 and Table 1) and Raman spectroscopy (Fig. 6).

Whatever the anodizing conditions (electrolyte composition and voltages), XPS survey spectra realized on the processed samples show the presence of carbon from contamination,

oxygen, magnesium under oxidized form (B.E. of Mg 2p in the range 50.8-51.2 eV) and aluminium under oxidized form (B.E. of Al 2p in the range 74.1 and 74.9 V) coming from the oxidation of the Al-rich intermetallic phases of the alloy. According to the Raman spectra (Fig. 6), both MgO (1088-1096 cm^{-1}, 978 cm^{-1} [23][24]) and $Mg(OH)_2$ (280 cm^{-1}[25]) are present at 40 V and 75 V whatever the electrolyte composition.

In the case of silicate-containing and fluoride-containing electrolytes, XPS results (Fig. 5) confirm that silicon and fluorine are respectively incorporated in the corresponding layers both in the thin layer grown at 40 V and in the top layer at 75 V. Si/Mg and F/Mg atomic ratio were evaluated thanks to the relation between the integral intensities of Mg 2p, Si 2p and F 1s peaks, the Scofield factors [26] ($\sigma_{Mg} = 0.33$, $\sigma_{Si} = 0.82$, $\sigma_F = 4.4$) and the inelastic mean free paths calculated from the Tanuma's formula [27] ($\lambda_{Mg2p} = 27$ Å , $\lambda_{Si2p} = 26$ Å , $\lambda_{F1s} = 17$ Å). Si/Mg ratio was estimated to 0.4 in the thin layer at 40 V and 0.5 in the top layer at 75 V. F/Mg was estimated to 0.1 both in the thin layer at 40 V and in the top layer at 75 V.

In the case of anodizing up to 40 V, the F 1s and Mg 2p peaks can be well decomposed by using only one component The Si 2p component at 102.5 eV can be assigned to an octahedral environment of Si such as observed in $MgSiO_3$ compound [28]. The F 1s component at 685.6 eV is more difficult to interpret, and could indicate the presence of $Mg(OH)_{2-x}F_x$ species already observed as corrosion products formed on Mg in alkaline fluoride solutions [29- 30].

For the 75 V anodized layer grown under few minutes of micro-arc regime, a second kind of fluoride and silicate appears in the top layer, which is shown by the appearance of a second component in the XPS peak, indicating a modification of the chemical compounds in which fluorides or silicates are incorporated. In the case of Si, the second component of Si 2p at 103.6 eV can be attributed to a tetrahedral environment of Si such as observed in Mg_2SiO_4 [28]. This result is corroborated by the Raman band between 850 cm^{-1} and 900 cm^{-1}, characteristic for silicates in tetrahedral configuration in Fig. 6b [31, 32]. In the case of F, the second F 1s component at 686.6 eV, could be assigned to more strongly bound fluorides such

as in MgF_2, that is confirmed by the presence at 75 V of a characteristic band for MgF_2 (295 cm^{-1}) in the Raman spectra [33, 34].

3.2. Electrochemical behaviour

In immersion in ASTM water, the corrosion potential of the untreated AZ91 alloy reaches a value around -1.4 V, and becomes very noisy from 8 to 10 h of immersion which is the sign of pitting phenomenon, as observed in previous studies [10] (Fig.7).

In these conditions, the corrosion potential of anodized samples is systematically lower than the one measured on the untreated alloy, and remains stable along the immersion time. These low values of corrosion potential are consistent with the decrease in the cathodic current densities, recorded in the potentiodynamic curves in the Figure 8a and c, which indicates a significant inhibition of the cathodic reaction of water reduction. The cathodic inhibition effect is slightly more important for alloys anodized up to 40 V, and on the samples anodized with the silicate-containing electrolyte.

Concerning the behaviour on the anodic branch (Fig. 8b and d), all the anodized layers permit to inhibit the pitting phenomenon that is observed on untreated sample, as revealed by the apparition of a passivation plateau. Nevertheless, the current density on the plateau of the 40 V-anodized samples remains relatively high at 10^{-5} A cm^{-2}, and the length of the passive layer does not exceed 500 mV (Fig. 8c). For the 75 V-anodized layer, the passive potential range can reach 800 mV (Fig. 8d). At 75 V, the effect on anodic branch of the fluoride and silicate addition in the anodizing electrolyte is slightly different. In fact, the fluoride-enriched electrolyte allows stabilizing a passive state over a large potential range (until -0.6 V /SCE), whereas the silicate-containing electrolyte induces the formation of a more passive layer (with a passive current about 10^{-6} A cm^{-2}), stable over a shorter potential range.

In order to characterize the electrochemical interface of the different anodized samples, electrochemical impedance spectra were regularly recorded during 24 h of immersion. Fig. 9

displays the EIS spectra measured after a short immersion time, 2 hours, and a long immersion time, 22 hours.

For 40V-anodized samples, the Bode diagrams displayed in Fig. 9a, present similar shapes whatever the anodizing electrolyte and the immersion time in the corrosive water. This impedance data can be interpreted by two phenomena described using the electrical equivalent circuit depicted in Fig. 10a:

- At medium frequency, the first phenomenon has a time constant (R_{MF}, Q_{MF}) of about 5 10^{-1} Hz, and can be assigned to the charge transfer across the thin passive layer or directly at the metal/electrolyte interface at the bottom of the layer porosities. In all electrolytes, the capacitance of the electrochemical interface, represented by a Q value, is approximately the same around 10 $\mu S\, s^n\, cm^{-2}$.
- The second one at low frequency is attributed to a diffusion process of Mg^{2+} and OH^- ions in a finite region near the metal surface, and noted O in the equivalent circuit [35]. The O-diffusion component is mathematically described as follows : $Z_O(\omega) = \left\{ \frac{1}{Y_O \sqrt{j\omega}} \right\} \tanh\left[B\sqrt{j\omega}\right]$. The Y_O and B parameters define the diffusion resistance R_D of ions in the finite region which is calculated by the relation: $R_D = B/Y_O$.

As can be seen in Table 2, whatever the electrolyte, R_{MF} and R_D of the thin 40 V-anodized layers increase with immersion time, which explains the increase in the modulus measured at low frequency in the EIS spectra (Fig. 9b). The increase of the charge transfer resistance and the diffusion resistance can be explained at the open-circuit potential by a process of self-sealing of the thin anodized layer by either, the formation of corrosion products, or a modification of the initial anodized layer.

After anodizing up to 75 V in KOH electrolyte, the impedance spectra of anodized sample is comparable to the one anodized up to 40 V. The impedance data can obviously be well fitted with the equivalent circuit of Fig. 10a, and give some similar results to the one obtained with

40V-anodized layer (the fitted values are given in supplementary material). This is consistent with the stop in the layer growth as the dielectric voltage breakdown is reached.

Even if the layers fomed up to 75 V in KOH/KF and KOH/Na_2SiO_3 electrolytes are thicker than the ones anodized up to 40 V, the impedance spectra profiles remain quite comparable to the ones recorded after anodizing up to 40 V, as can be observed in Fig. 9. However, the global resistance value, characterized by the Z modulus at low frequency, is higher. Moreover the Bode representation exhibits an additional time constant at high frequency (around 10^4 to 10^5 Hz), especially during the first hours of immersion, as can be seen in Fig. 9c.

So, the impedance of 75 V- anodized layer immersed in ASTM water can be fitted with the equivalent circuit described in Fig. 10b, where:

- The high frequency part of the spectra (R_{HF}, Q_{HF}) is assigned to a very rough top layer, containing many macro cracks and holes, as can be observed in Fig. 4c, d. In all cases, the fits using the equivalent circuit verify the low impedance of the high frequency phenomenon, as shown by the R_{HF} values reported in the Table 3, probably due to the very rough and cracked morphology of the top layer.
- The medium frequency part (R_{MF}, Q_{MF}) is attributed to the charge transfer across the internal zone of the layer or directly at the metal/electrolyte interface. This internal zone, containing the thin layer in contact with the substrate and an intermediate layer with small porosities, is defined with the help of the cross section displayed in Fig. 10b. Unfortunately, in this case, it is not possible to distinguish the relaxation constants due to the thin internal layer and the intermediate layer.

As can be noted in Table 3 and consistently with in-situ impedance measurements, the 75V-anodized layer formed in KOH/KF electrolyte shows a higher internal zone resistance (R_{MF}) and a higher top layer resistance (R_{HF}) than the layer formed in KOH/Na_2SiO_3 electrolyte for short immersion time (2 h). So despite the fact that the silicate-containing layer is considerably thicker than the fluoride containing layer, the difference of resistances seems to

be due to the compactness or porosity and especially the opened porosities towards the metal surface.

With increasing of the immersion time, the behaviour of 75 V-anodized layer in KOH/KF and KOH/Na_2SiO_3 electrolytes is significantly different. In fact, with fluoride additives, the resistance of the internal zone, R_{MF}, and the top layer, R_{HF}, drastically decrease in corrosive water; they are approximately divided by a 10 factor after 22 h of immersion. On the opposite, with silicate additive, silicate-containing layer undertakes an increase of the resistances of the two layers, up to 100 kΩ cm^2 for the internal zone resistance, R_{MF}, and 40 Ω cm^2 for the top layer resistance. It seems that the fluoride-containing layer undergoes a dissolution in this corrosive medium, associated with an opening of the porosities revealed by the decrease of the diffusion resistance R_D. On the contrary, the silicate-containing layer appears to be sealed with time of immersion which results in an increase in R_D and R_{MF}.

4. Discussion

By combining in-situ high-voltages electrochemical measurements and post-treatment surface characterizations, the major role of additives to a KOH-based electrolyte could be highlighted. They actually act both on the dielectric breakdown voltage and on the further growth of the coatings under micro-arc regime. Whereas the thickness and the morphology of the anodized layers formed under classical anodizing (before discharges initiation) are similar whatever the electrolyte composition, the electrical parameters drastically depend on the presence and the nature of the additives (Fig. 2). Especially, the increase of the resistive part of the thin anodized layer can be corroborated to the presence, besides the major constituent $Mg(OH)_2$, of fluorides maybe under the form of $Mg(OH)_{2-x}F_x$ or silicates under the form of $MgSiO_3$. This incorporation in the brucite layer increases its compactness as shown by SEM observations, but also modifies its electric properties. Particularly, the presence of $MgSiO_3$ or $Mg(OH)_{2-x}F_x$ compounds in the layer is susceptible to reduce the intercalation and adsorption of water in the brucite structure that is responsible of the relatively important conductivity of

hydrated brucite, as measured by some authors [36]. It is important to mention that the incorporation of silicates (Si/Mg = 0.4) in this layer is more efficient than the incorporation of fluorides (F/Mg = 0.1), because of the more insoluble properties of magnesium silicates than magnesium fluorides.

The properties obtained with the silicate-containing layer permit to reach the dielectric breakdown at a lower voltage than the one with fluoride-containing layer, as shown in Fig. 1. This result is interesting to consider for further industrial applications for which energy consumption is important.

Then, during the arcing phenomenon, the chemical compositions of the layers change because of the high temperature reached at the interface. The silicate-containing electrolyte induces the formation of forsterite, Mg_2SiO_4, a simple form of olivine mineral, with a global composition of about Mg/Si=0.5 in at% in the layer. The fluorides presence provokes the appearance of MgF_2 in the layer, with F/Mg=0.1 in the layer. The second characteristic of the layer formed during the arcing is that the silicate–containing layer is much thicker than the fluoride-containing one. However, the electric discharges in a thick and dense oxide layer can rapidly produce macro cracks due to internal mechanical stress, or holes because of the discharge cone across the layer. Therefore, the thick layer can become inefficient to form a good protection against corrosion in these conditions. Nevertheless, the physicochemical parameters of the compounds formed in the layer, especially their insolubility in the electrolyte, remain the key parameters to manage the make-up of the coating during the arcing phenomenon and its further degradation in corrosive environment.

Concerning the electrochemical behaviour in corrosion conditions of the coated materials, the corrosion resistance of the 40 V-anodized layers remains moderate. Nevertheless, according to the EIS analysis, the global resistance of the layer and the diffusion resistance increase with immersion time which suggests a mechanism of sealing of the porosities during the corrosion process. This mechanism stabilises a passive state of the AZ91 alloy on a relatively large potential range according to the potentiodynamic curves.

In our corrosion conditions, this phenomenon of self-sealing of coating during the corrosion process is enhanced in the case of the 75 V-anodized layer in the silicate-containing electrolyte, as shown by the evolution of resistances in Table 2. Inversely, the fluoride-containing layer anodized up to 75 V seems to be partially dissolved after 22 h immersion, because of the decrease of the diffusion resistances. In fact, two reasons can be the starting point of the sealing process of the layer:

- the formation of corrosion products which fill the porosities of the layer,
- the hydrolysis of a part of the coating.

In the case of fluoride-containing layer, the hydrolysis of MgF_2 in the corrosive medium leads to the dissolution of the layer. In contrary, Mg_2SiO_4 is very insoluble and can form in contact with water voluminous compounds of serpentine type and brucite, as follows [37]:

$2\ Mg_2SiO_4 + 3H_2O \rightarrow Mg_3Si_2O_5(OH)_4 + Mg(OH)_2$

5. Conclusions

In-situ electrochemical measurements and post-treatment analyses reveal that the nature of the electrolyte modifies the composition and the morphology of a first oxidized layer, grown under a classical anodizing regime before the occurrence of the dielectric breakdown. Indeed, the incorporation of fluorides or silicates respectively under $Mg(OH)_{2-x}F_x$ form and $MgSiO_3$ form could be highlighted. It induces a resistance increase of the interface and influences the dielectric breakdown voltage, occurring at a specific value of capacitance of the first grown dielectric layer.

During the discharges regime, the coating further grows only in additive-containing electrolytes. Fluorides and silicates from the bath are incorporated under MgF_2 or Mg_2SiO_4 forms.

The electrochemical behavior of the anodized layer is mostly determined by a sealing mechanism of porosities. This self-sealing can be due to the formation of corrosion products in porosities or by a hydrolysis phenomenon of the compounds of the layer, as Mg_2SiO_4. In

contrary, the hydrolysis of fluoride-containing layer weakens the protective behavior of the layer.

Acknowledgements

This study was performed in the framework of the European Clean Sky Joint Undertaking within the Co-Proclam project (Grant n° 270589). The participation of Liebherr aerospace (LTS), Eurocopter, Turbomeca and Agusta Westland companies as GTI members has been deeply appreciated.

References

[1] J.E. Gray, B. Luan, J. Alloys Comp 336 (2002) 88.

[2] L. Kouisni, M. Azzi, M. Zertoubi, F. Dalard, S. Maximovitch, Surf. Coat. Technol. 185 (2004) 54.

[3] K.Z. Chong, T.S. Shih, Materials Chemistry and Physics 80 (2003), 191.

[4] J. Horner, Met. Finish. 88 (1990), 76.

[5] H.A. Evangelides, Met. Finish. 7 (1951), 56.

[6] J.W. Schultze, M.M. Lohrengel, Electrochim. Acta 45 (2000), 2499.

[7] S. Verdier, M. Boinet, S. Maximovitch, F. Dalard, Corros. Sci. 47 (2005), 1429.

[8] Z. Shi, G. Song, A Atrens, Corros. Sci. 48 (2006), 1939.

[9] P. Bala Srinivasan, J. Liang, C. Blawert, M.Störmer, W. Dietzel, Appl. Surf. Sci. 255 (2009), 4212.

[10] C.E. Barchiche, E. Rocca, C. Juers, J. Hazan, J. Steinmetz, Electrochim. Acta 53 (2007), 417.

[11] A. Ghasemi, V.S. Raja, C. Blawert, W. Dietzel, K.U. Kainer, Surf. Coat. Technol. 204 (2010), 1469.

[12] A. Ghasemi, V.S. Raja, C. Blawert, W. Dietzel, K.U. Kainer, 202 (2008), 3513.

[13] J. Liang, B. Guo, J. Tian, H. Liu, J. Zhou, T. Xu, Appl. Surf. Sci. 252 (2005), 345.

[14] J. Liang, L. Hu, J. Hao, Appl. Surf. Sci 253 (2007), 4490.

[15] H. Duan, C. Yan, F. Wang, Electrochim. Acta 52 (2007), 3785.

[16] C.E. Barchiche, D. Veys-Renaux, E. Rocca, Surf. Coat. Technol. 205 (2011), 4243.

[17] D. Veys-Renaux, E. Rocca, G. Henrion, Electrochem. Com. 31 (2013), 42.

[18] D.A. Shirley, Phys. Rev. B **5 (**1972), 4709.

[19] Annual book of ASTM standards, Copyright ASTM, PA, 1986.

[20] B.A. Boukamp, Solid State Ionics 20 (1986), 31.

[21] B. Hirschorn, M. E. Orazem, B. Tribollet, V. Vivier, I. Frateur, Marco Musiani, Electrochim. Acta 55 (2010), 6218.

[22] S. Dunleavy, J.A. Curran, T.W. Clyne, Appl. Surf. Sci. 268 (2013), 397.

[23] H.K. Böckelmann, R.G. Schlecht, Phys. Rev. 10 (1974), 5225.

[24] K. Ishikawa, N. Fujima, H. Komura, J. Appl. Phys. 57 (1985), 973.

[25] E. Rocca, C. Juers, J. Steinmetz, Corr. Sci. 52 (2010), 2172.

[26] J.H. Scofield, J. Electr. Spectrosc. and Rel. Phenom. 8 (1976), 129.

[27] S. Tanuma, C.J. Powell, D.R. Penn, Surf. Int. Ana. 20 (1993), 77.

[28] R. Brambilla, C. Radtke, João H. Z. Dos Santos, Márcia S. L. Miranda, Journal of Sol-Gel Science and Technology 51 (2009), 70.

[29] E. Gulbrandsen, J. Tafto, A. Olsen, Corros. Sci 34 (1993), 1423.

[30] P.M. Bradford, B. Case, G. Dearnaley, J.F. Turner and L.S Woolsley, Corros. Sci 16 (1976), 747.

[31] P. McMillan, Am. Mineral. 69 (1984), 622.

[32] A. Chrissanthopoulos, N. Bouropoulos, S.N. Yannpoulos, Vibration. Spectro. 48 (2008), 118.

[33] R.S. Krishnan, R.S. Katiyar, J. Phys. 26 (1965), 627.

[34] S.P.S. Porto, P.A. Fleury, T.C. Damen, Phys. Rev. 154 (1967), 522.

[35] D.R. Franceschetti, J.R. Macdonald, J. Electroanal. Chem. 100 (1979), 583.

[36] J. Gasc, F. Brunet, N. Bagdassarov, V. Morales-Florez, Phys. Chem. Miner 38 (2011), 543.

[37] C. Mével, Comptes Rendus Geoscience 335 (2003), 825.

Tables

		F 1s (1)		F 1s (2)		Si 2p (1)		Si 2p (2)	
Electrolyte		**B.E. /eV**	**FWHM**	**B.E. /eV**	**FWHM**	**B.E. /eV**	**FWHM**	**B.E. /eV**	**FWHM**
KOH/KF	40V	685.6	1.7	-	-	-	-	-	-
	75V	685.6	1.7	686.6	1.8	-	-	-	-
KOH/Na_2SiO_3	40V	-	-	-	-	102.5	1.7	-	-
	75V	-	-	-	-	102.5	1.8	103.6	1.8

Table 1: Binding energies (B.E.) and full width at half-maximum (FWHM) of the different components of the XPS core-level lines (examples shown in Figure 5).

Electrolyte	**KOH**		**KOH/KF**		**KOH/Na_2SiO_3**	
Immersion time /h	2	22	2	22	2	22
R_{MF} / Ω cm²	3380	9220	3720	11650	3090	7380
R_D / Ω cm²	1760	7410	2150	3330	2030	8020

Table 2: Evolution of electrical resistances of 40 V-anodized layer in the different electrolytes, versus immersion time in ASTM water, calculated from the fitting of EIS data by using the equivalent circuit of Fig 10a.

Electrolyte	**KOH/KF**		**KOH/Na_2SiO_3**	
Immersion time /h	2	22	2	22
R_{HF} / Ω cm²	980	60	8	39
R_{MF} / Ω cm²	128500	12980	25580	105400
R_D / Ω cm²	64430	4170	20090	68430

Table 3: Evolution of electrical resistances of 75 V-anodized layer in the different electrolytes, versus immersion time in ASTM water, calculated from the fitting of EIS data by using the equivalent circuit of Fig 10b.

Figure captions

Figure 1: Potentiodynamic curves (0-75 V) recorded at 100 mV s^{-1} on AZ91 alloys in KOH (a), KOH/KF 0.5 M (b), KOH/Na_2SiO_3 0.5 M (c).

Figure 2: Electric parameters calculated from continuous impedance measurements during the potential scan (0- 75 V) at 100 mV s^{-1} at 5000Hz: R (a), 1/C (b).

Figure 3: Cross-section and surface observations of 40 V-anodized layer on AZ91 in KOH electrolyte (cross-section (a), surface (b)), in KOH/KF electrolyte (surface, (c)) and in KOH/Na_2SiO_3 electrolyte (surface, (d)).

Figure 4: Cross-section and surface observations of 75 V-anodized layer on AZ91 in KOH/KF electrolyte (cross-section (a), surface (b)), and in KOH/Na_2SiO_3 electrolyte (cross-section (c), surface (d)).

Figure 5: F 1s and Si 2p XPS experimental core level lines and their decomposition after anodizing of AZ91 alloys in KOH/KF up to 40 V (a), up to 75 V (b) and in KOH/Na_2SiO_3 up to 40 V, up to 75 V.

Figure 6: Raman spectra recorded on AZ91 alloys processed in KOH, KOH/ KF and KOH/Na_2SiO_3 up to 40 and 75 V in the spectral range of a) 160 – 350 cm^{-1} and b) 750 – 1200 cm^{-1}.

Figure 7: Corrosion potentials of 40 V-anodized layer (a) and 75 V-anodized layer on AZ91 alloy measured during 22 h immersion in ASTM water.

Figure 8: Cathodic and anodic potentiodynamic curves of 40 V-anodized layer (a, b) and 75 V-anodized layer (c,d) on AZ91 alloy after 22 h immersion in ASTM water.

Figure 9: Experimental EIS spectra of 40 V-anodized layer (a, b) and 75 V-anodized layer (c,d) on AZ91 alloy, after 2 h of immersion (a, c) and 22 h of immersion (b, d) in ASTM water.

Figure10: Equivalent circuits used to fit EIS spectra of 40 V-anodized layers (a) and 75 V-anodized layers (b) immersed in ASTM water.

Figures

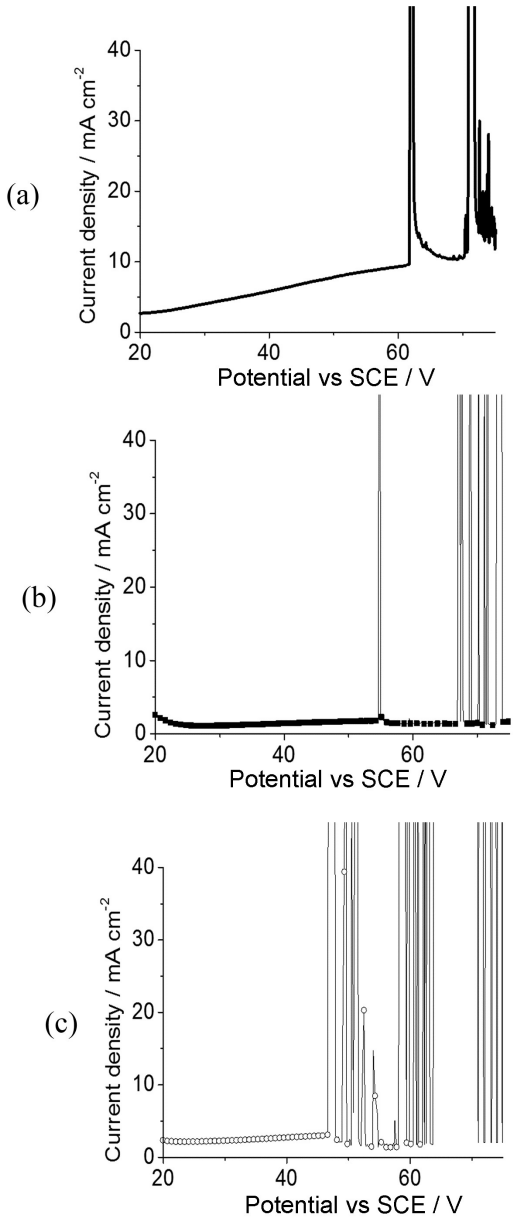

Figure 1: Potentiodynamic curves (0-75 V) recorded at 100 mV s^{-1} on AZ91 alloys in KOH (a), KOH/KF 0.5 M (b), KOH/Na_2SiO_3 0.5 M (c).

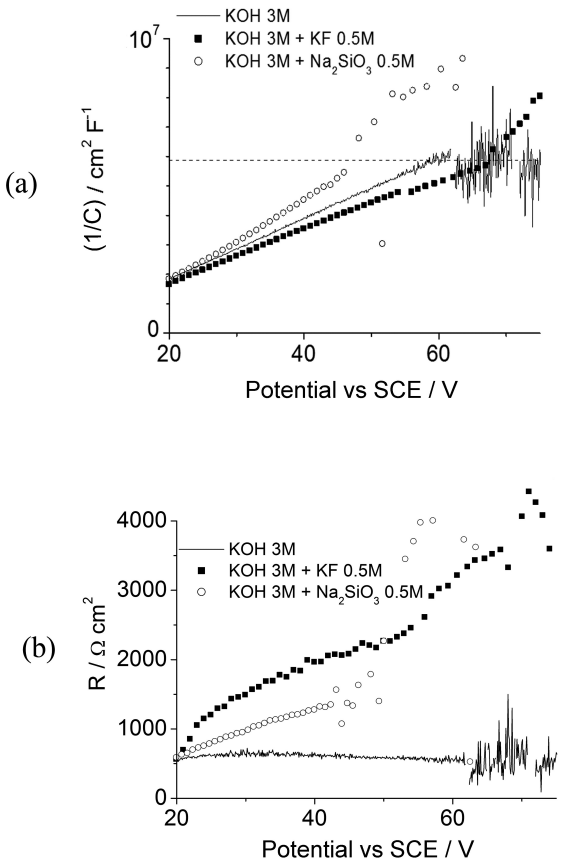

Figure 2: Electric parameters calculated from continuous impedance measurements during the potential scan (0- 75 V) at 100 mV s^{-1} at 5000Hz: R (a), 1/C (b).

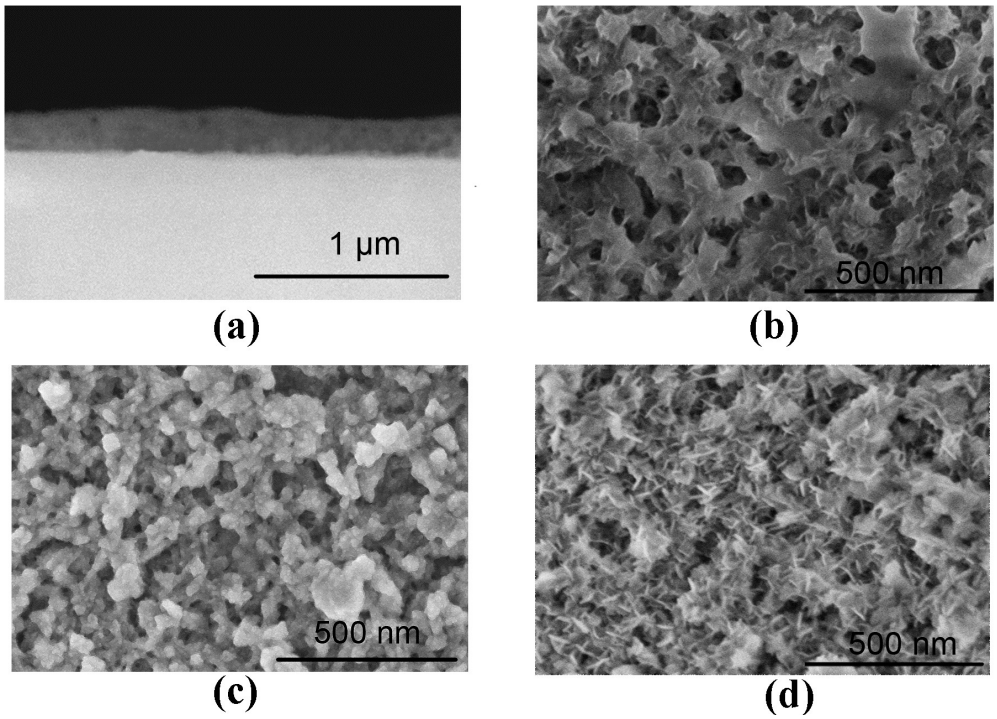

Figure 3: Cross-section and surface observations of 40 V-anodized layer on AZ91 in KOH electrolyte (cross-section (a), surface (b)), in KOH/KF electrolyte (surface, (c)) and in KOH/Na_2SiO_3 electrolyte (surface, (d)).

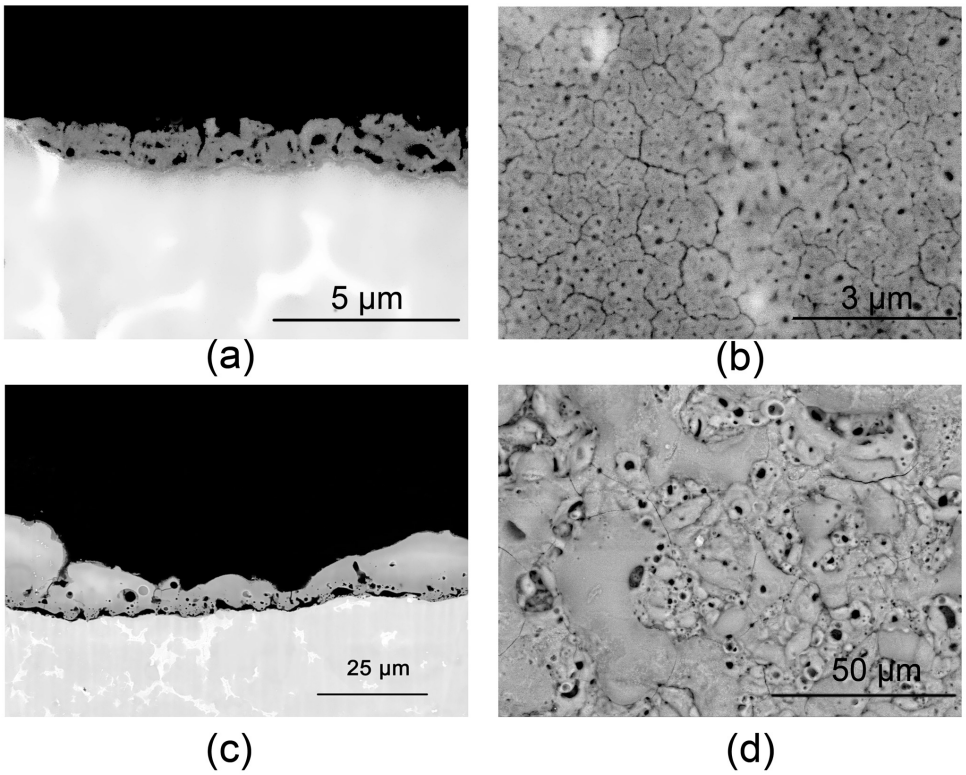

Figure 4: Cross-section and surface observations of 75 V-anodized layer on AZ91 in KOH/KF electrolyte (cross-section (a), surface (b)), and in KOH/Na_2SiO_3 electrolyte (cross-section (c), surface (d)).

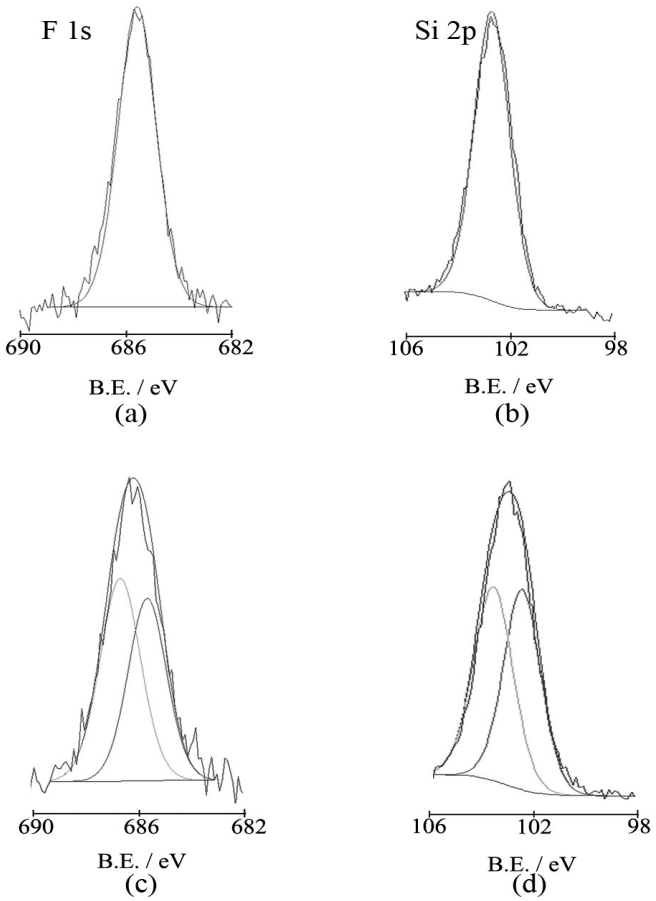

Figure 5: F 1s and Si 2p XPS experimental core level lines and their decomposition after anodizing of AZ91 alloys in KOH/KF up to 40 V (a), up to 75 V (b) and in KOH/Na_2SiO_3 up to 40 V, up to 75 V.

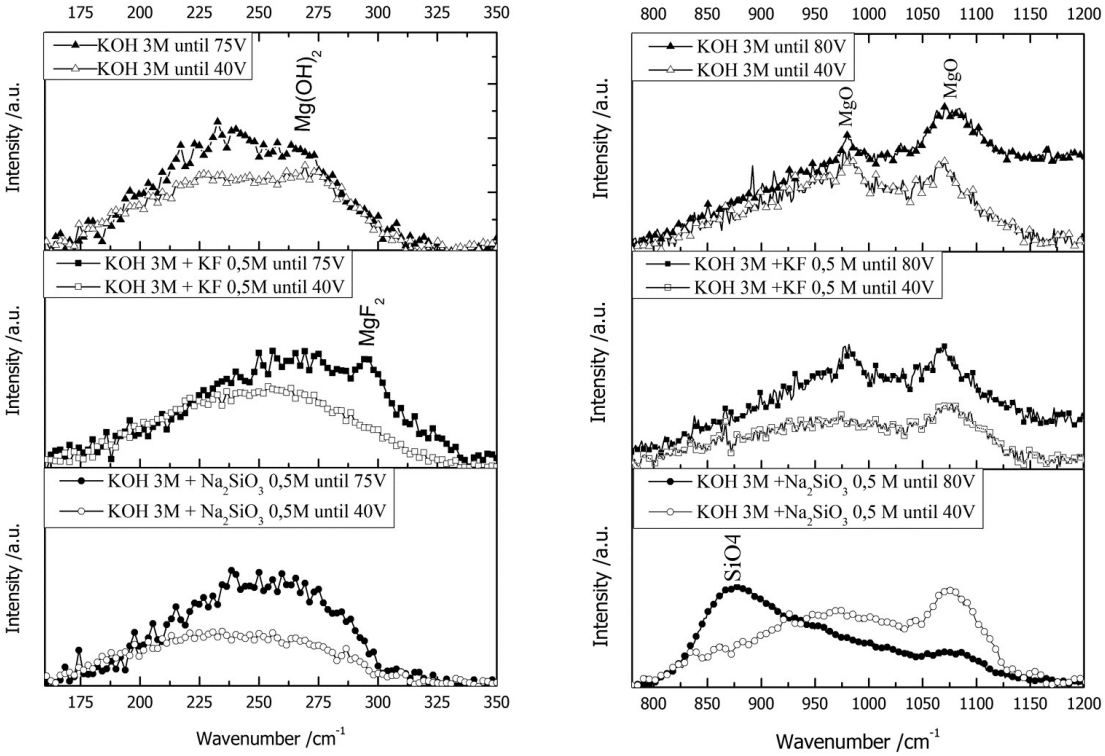

Figure 6: Raman spectra recorded on AZ91 alloys processed in KOH, KOH/ KF and KOH/Na_2SiO_3 up to 40 and 75 V in the spectral range of a) 160 – 350 cm^{-1} and b) 750 – 1200 cm^{-1}.

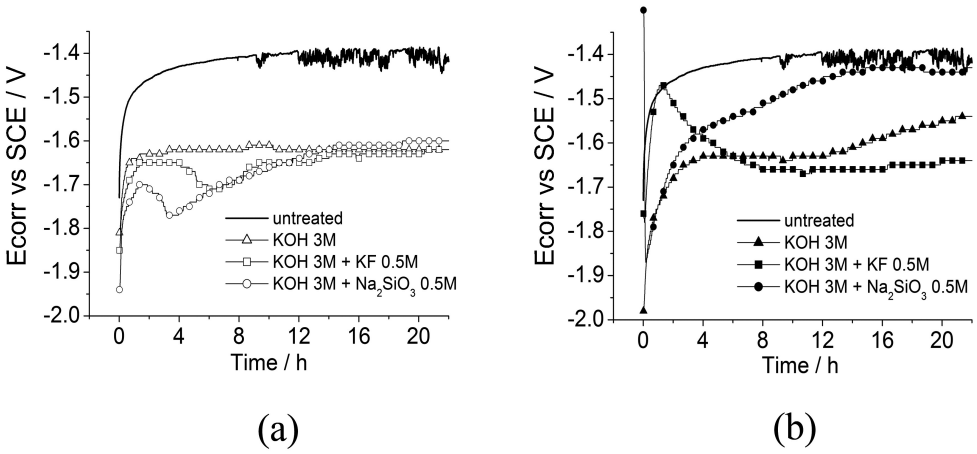

Figure 7: Corrosion potentials of 40 V-anodized layer (a) and 75 V-anodized layer on AZ91 alloy measured during 22 h immersion in ASTM water.

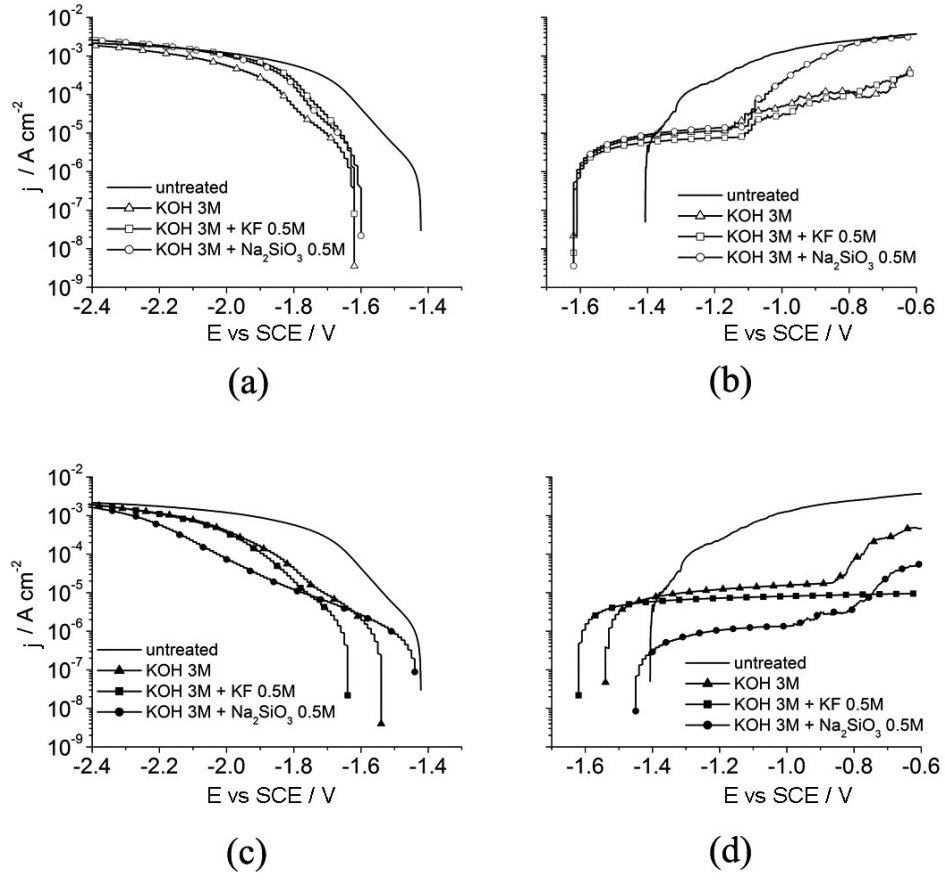

Figure 8: Cathodic and anodic potentiodynamic curves of 40 V-anodized layer (a, b) and 75 V-anodized layer (c,d) on AZ91 alloy after 22 h immersion in ASTM water.

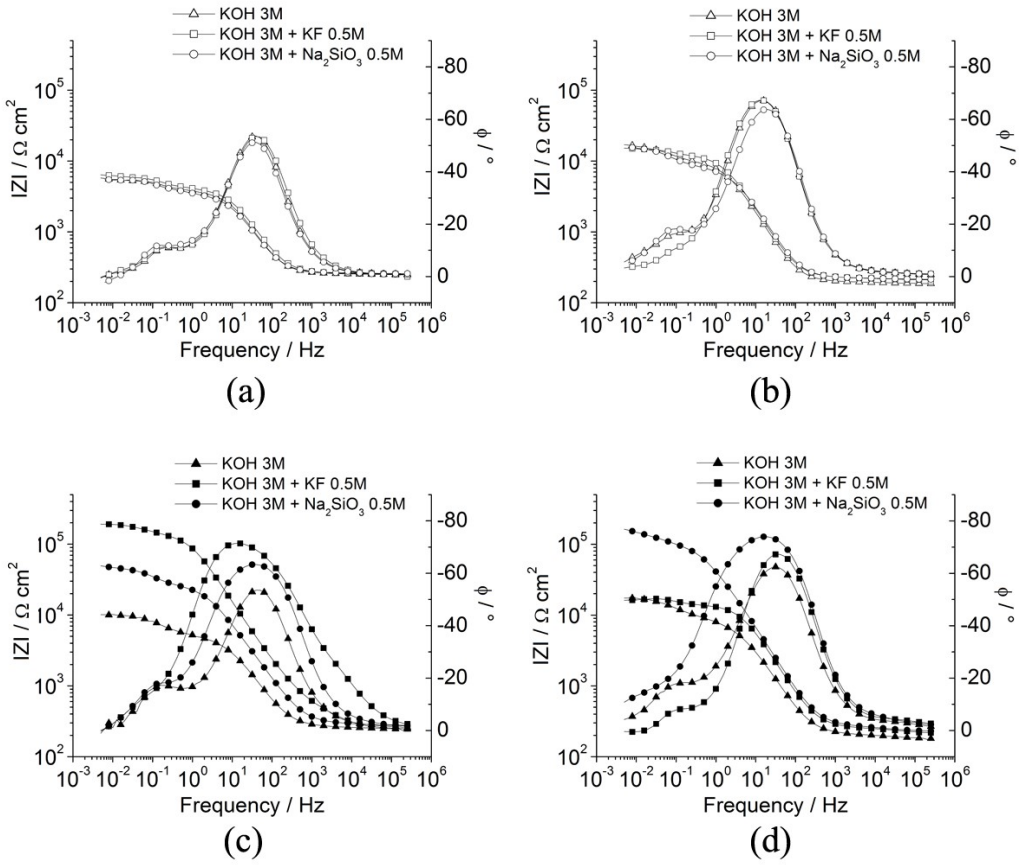

Figure 9: Experimental EIS spectra of 40 V-anodized layer (a, b) and 75 V-anodized layer (c,d) on AZ91 alloy, after 2 h of immersion (a, c) and 22 h of immersion (b, d) in ASTM water.

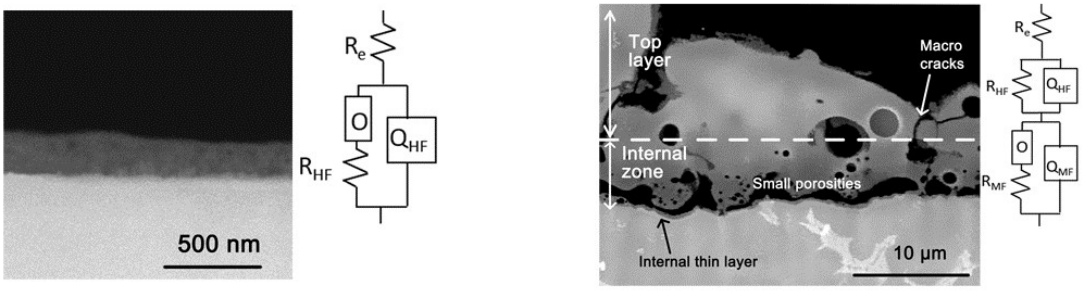

Figure10: Equivalent circuits used to fit EIS spectra of 40 V-anodized layers (a) and 75 V-anodized layers (b) immersed in ASTM water.

Supplementary material

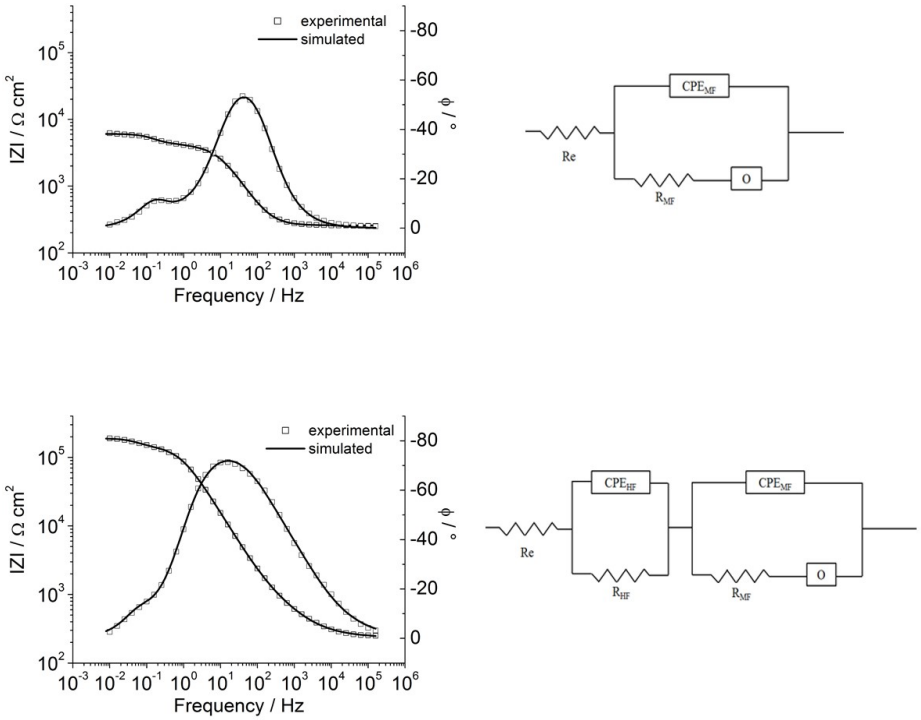

Figure: Examples of simulated EIS diagrams with the corresponding equivalent circuits after 2 h immersion in ASTM water for AZ91 anodized in KOH/KF up to 40V (a) and up to 75V (b).

	40V						75V					
	KOH		KOH/KF		KOH/Na_2SiO_3		KOH		KOH/KF		KOH/Na_2SiO_3	
	2H	22H	2H	22H	2H	22H	2H	22H	2H	22H	2H	22H
Re $\Omega\ cm^2$	253	192	257	221	262	221	256	198	243	211	281	226
CPE_{HF} $\mu S\ s^n\ cm^{-2}$	-	-	-	-	-	-	-	-	20	25	6	2
R_{HF} $\Omega\ cm^2$	-	-	-	-	-	-	-	-	980	60	8	39
n	-	-	-	-	-	-	-	-	0.58	0.57	0.86	0.79
CPE_{MF} $\mu S\ s^n\ cm^{-2}$	8	12	7	11	9	10	7	9	1	4	4	4
R_{MF} $\Omega\ cm^2$	3378	9223	3727	11650	3092	7384	4609	8284	128500	12978	25580	105400
n	0.90	0.91	0.89	0.91	0.89	0.91	0.86	0.86	0.91	0.92	0.84	0.88
Y_0 $\mu S\ s^{1/2}\ cm^{-2}$	891	426	813	801	820	354	373	279	40	463	114	83
B $s^{1/2}$	1.57	3.16	1.75	2.67	1.66	2.83	1.88	2.47	2.59	1.93	2.28	5.69
R_D $\Omega\ cm^2$	1765	7407	2152	3332	2029	8017	5048	8836	64428	4168	20088	68431

Table: Electrical parameters calculated from the fitting of EIS data by using the equivalent circuits described in Figure 10.